Structural basis for late maturation steps of the human mitoribosomal large subunit

Authors: Miriam Cipullo[1,2,†], Genís Valentín Gesé[3,†], Anas Khawaja[1,2], B. Martin Hällberg[3,4,*], Joanna Rorbach[1,2,*]

Affiliations:

[1] Department of Medical Biochemistry and Biophysics, Division of Molecular Metabolism, Karolinska Institutet, Solnavägen 9, 171 65 Solna, Sweden

[2] Max Planck Institute Biology of Ageing - Karolinska Institutet Laboratory, Karolinska Institutet, Stockholm, Sweden

[3] Department of Cell and Molecular Biology, Karolinska Institutet, Solnavägen 9, 171 65 Solna, Sweden

[4] Centre for Structural Systems Biology (CSSB) and Karolinska Institutet VR-RÅC, Notkestrasse 85, 22607 Hamburg, Germany.

†Joint First Authors

*Correspondence to:

B. Martin Hällberg

Address: Department of Cell and Molecular Biology, Karolinska Institutet, Solnavägen 9, 171 65 Solna, Sweden

Email: martin.hallberg@ki.se

Joanna Rorbach

Department of Medical Biochemistry and Biophysics, Research Division of Molecular Metabolism, Karolinska Institutet, Solnavägen 9, 171 65 Solna, Sweden

Email: joanna.rorbach@ki.se

Abstract

Mitochondrial ribosomes (mitoribosomes) synthezise a critical set of proteins essential for oxidative phosphorylation. Therefore, their function is vital to cellular energy supply and mitoribosomal defects give rise to a large and diverse group of human diseases [1]. The architecture of mitoribosomes is strikingly different from that of their bacterial and eukaryotic cytosolic counterparts and display high divergence between species [2–6]. Mitoribosome biogenesis follows distinct molecular pathways that remain poorly understood. Here, we determined the cryo-EM structures of mitoribosomes isolated from human cell lines with either depleted or overexpressed mitoribosome assembly factor GTPBP5. This allowed us to capture consecutive steps during mitoribosomal large subunit (mt-LSU) biogenesis that involve normally short-lived assembly intermediates. Our structures provide important insights into the last steps of 16S rRNA folding, methylation and peptidyl transferase centre (PTC) completion, which require the coordinated action of nine assembly factors. We show that mammalian-specific MTERF4 contributes to the folding of 16S rRNA, allowing 16S rRNA methylation by MRM2, while GTPBP5 and NSUN4 promote fine-tuning rRNA rearrangments leading to PTC formation. Moreover, our data reveal an unexpected role for the elongation factor mtEF-Tu in mt-LSU assembly, in which mt-EF-Tu interacts with GTPBP5 in a manner similar to its interaction with tRNA during translational elongation. Together, our approaches provide detailed understanding of the last stages of mt-LSU biogenesis that are unique to mammalian mitochondria.

Main

Mammalian mitoribosomes assemble in a multi-step process that includes the maturation of two ribosomal RNAs (rRNAs; 12S and 16S), a structural tRNA, and incorporation of 82 mitoribosomal proteins (MRPs) [7]. Multiple assembly factors, many specific to mammalian mitochondria, assist in the mitoribosome assembly process. A growing number of studies in recent years have shown that a family of GTP-binding proteins (GTPBPs) is crucial for mammalian mitoribosome assembly [8–13]. Among these GTPBPs, GTPBP5 participates in the late steps of large subunit (mt-LSU) maturation, and its deletion leads to severe translational defects [8,11].

To understand the molecular basis for the late stages of human mitochondrial mt-LSU assembly, we used single-particle electron cryomicroscopy (cryo-EM) to determine the structure of an mt-LSU intermediate isolated from GTPBP5-deficient cells (GTPBP5^{KO}). In addition, we determined the cryo-EM structure of a GTPBP5-bound mt-LSU intermediate immunoprecipitated from cells expressing a tagged variant of GTPBP5 (GTPBP5^{IP}).

Composition of the GTPBP5^{KO} and GTPBP5^{IP} mt-LSU assembly intermediates

Both the GTPBP5^{KO} and GTPBP5^{IP} mt-LSU assembly-intermediates reveal several trapped assembly factors: the MTERF4-NSUN4 complex, MRM2, MTG1 and the MALSU1:L0R8F8:mt-ACP module (Fig. 1a,b, Extended Data Fig. 1 and 2). Furthermore, the GTPBP5^{IP} mt-LSU structure features GTPBP5 and the mitochondrial elongation factor mtEF-Tu (Fig. 1b, Extended Data Fig. 2). Comparing the GTPBP5^{KO} and the GTPBP5^{IP} mt-LSU intermediates with the mature mt-LSU [14] reveals two crucial differences in the 16S rRNA conformation (Fig. 1c,d). First, in both GTPBP5^{KO} and GTPBP5^{IP} intermediates, MTERF4 in the MTERF4-NSUN4 complex, binds an immaturely folded region of the 16S domain IV. This region (C2548-G2631) – corresponding to helices H68, H69, and H71 of the mature mt-LSU – is folded into a novel intermediate rRNA helical structure, hereafter denoted helix-X (Fig. 1). The helix-X occupies a different position on the mt-LSU than H68-71 in the mature mt-LSU, where helices H68-71 and H89-90 jointly form the peptidyl-transferase centre (PTC) (Fig. 1d). MTERF4s binding of helix-X partly orders the disordered rRNA in the mt-LSU assemblies' subunit interface side (Extended Data Fig. 1) and thereby enables MRM2 to bind (Fig. 1d). Second, in the GTPBP5^{KO} – but not in the GTPBP5^{IP} – the junction between H89 and H90 of domain V is significantly different compared to the mature mitoribosome (Fig. 1c, d). Specifically, at the base of H89, one helical turn remains unfolded and instead forms a flexible loop in the GTPBP5^{KO} (Fig. 1d).

103 **MTERF4-NSUN4 complex steers the final steps of 16S rRNA folding and allows for**
104 **MRM2 binding**

105 The MTERF4-NSUN4 complex, previously shown to be essential for monosome
106 assembly [16,17], binds at the intersubunit interface in our GTPBP5^{KO} and GTPBP5^{IP} structures
107 (Fig. 1a, b). The C-terminal part of MTERF4 binds to NSUN4 close to the NSUN4 N-terminus
108 in a mixed hydrophobic-polar binding interface similar to earlier crystal structures of the
109 isolated complex [18,19] (Fig. 2a). NSUN4 was previously shown to m^{5}C-methylate the C1488
110 carbon 5 in 12S mt-rRNA [17]. In our structures, the active site of NSUN4 is turned towards the
111 mt-LSU core (Extended Data Fig. 3a), impeding methylation of the 12S mt-rRNA. Although
112 the methyl-donor S-adenosyl-methionine (SAM) is observed in the NSUN4 active site, no RNA
113 substrate is present. Furthermore, in the GTPBP5^{KO} and GTPBP5^{IP} structures, the MTERF4-
114 NSUN4 complex is bound and bent from two sides by uL2m. Specifically, a uL2m C-terminal
115 extension penetrates in between NSUN4 and MTERF4 to further stabilize the MTERF4-
116 NSUN4 binding interface and decreases the curvature of the MTERF4 solenoid relative to the
117 crystal structures (Fig. 2a). This reforming of the MTERF4 solenoid is necessary to bind the
118 helix-X rRNA region in the strongly positively charged concave side of MTERF4 (Extended
119 Data Fig. 3b). Here, MTERF4 forms an extensive network of contacts with helix-X that
120 stabilizes the association and promotes helix-X folding (Fig. 2b). The mature H71 base-pairing
121 is already formed within helix-X. Thus, by binding to helix-X, MTERF4 intiates the folding of
122 this 16S mt-rRNA region. Furthermore, it also exposes the A-loop, which is obstructed by H68,
123 H69, and H71 in the mature mt-LSU (Fig. 1d), thereby allowing MRM2 binding.

124 Similarly to a previously determined mt-LSU assembly intermediate [20] there is a
125 MALSU1-module positioned adjacent to uL14m in both the GTPBP5^{KO} and GTPBP5^{IP}
126 (Fig.1a,b). Furthermore, MTG1 (GTPBP7), which assists in late-stage mt-LSU maturation [21],
127 is bound in the vicinity of helix-X (Fig. 1a,b). MTG1 contacts the C-terminus of MALSU1
128 (Extended Data Fig. 4a) and the region encompassing A2554-U2602 of helix-X. This region
129 could not modelled due to the lower local resolution, but the contact is visible in the electron
130 density map (Extended Data Fig. 4b). Interestingly, the position of human MTG1 in our
131 structures differs significantly from its bacterial and trypanosomal counterparts ([3,22], Extended
132 Data Fig. 4c). Specifically, while in other systems MTG1 homologs contact the rRNA, reaching
133 out towards the PTC (Extended Data Fig. 4c), in the trapped intermediates described here
134 MTG1 is unlikely to induce pronounced conformational changes of the PTC or participate in
135 the recruitment/dissociation of assembly factors.

136 MRM2 2′-O-methylates U3039 in the 16S A-loop during mt-LSU assembly [23,24] and in
137 our GTPBP5^{KO} and GTPBP5^{IP} structures, MRM2 binds in the mt-LSU intersubunit interface
138 (Fig. 1a,b). It features two N-terminal α-helices followed by a canonical S-adenosyl-L-
139 methionine-dependent methyltransferase domain (SAM MTase) (Fig. 2c). In GTPBP5^{KO}, but
140 not in GTPBP5^{IP}, the two N-terminal α-helices extend from MRM2 and insert into the rRNA
141 core to thereby displace and retrieve the A-loop (16S mt-rRNA domain V) through a complex
142 interaction network (Fig. 2d,e). This places the 2′-hydroxyl of U3039 close to the ideal methyl-
143 acceptor position in the MRM2 active site (Fig. 2d). However, there is no density for either
144 SAM or S-adenosyl homocysteine (SAH) in the MRM2 active site and there is no apparent
145 density for a 2′-*O*-methyl on U3039 (Extended Data Fig. 5). Interestingly, G3040 that is 2′-*O*-
146 methylated by MRM3 [23,24], is methylated in our structures (Extended Data Fig. 5). Hence, 2′-
147 O-methylation by MRM3 takes place prior to MRM2 methylation in human mitoribosome
148 biogenesis.
149
150 **GTPBP5 promotes remodelling of the PTC**
151 GTPBP5 consists of a glycine-rich N-terminal domain (Obg-domain) and a C-terminal
152 GTPase domain (G-domain) (Fig. 3a). In our GTPBP5^{IP} structure, the G-domain has GTP in its
153 active site and is wedged between the L7/L12 stalk and the MALSU1 module (Fig. 1b and
154 Extended Data Fig. 6a). The Obg-domain protrudes into the PTC (Fig. 3b), thereby displacing
155 the A-loop from the MRM2 active site and expelling the MRM2 N-terminal α-helices from the
156 rRNA core (Fig. 3c), while the A-loop folds into the fully mature position (Fig. 3b3).
157 The protruding Obg-domain is positioned between H89 and H93 and occupies the space that
158 accommodates the acceptor arm of the A-site tRNA during translation (Extended Data Fig. 6b).
159 Hereby, GTPBP5 adopts a tRNA mimicry strategy, similar to ObgE of *E. coli* [25]. The Obg-
160 domain contains six glycine-rich sequence motifs that form antiparallel polyproline-II helices
161 (helices a–f) (Fig. 3b). Helices c and d bind the A-loop, while the loop between helices e and f
162 inserts into the major groove of H93. The loop between a and b inserts at the triple-junction
163 formed between H89-H90-H93 (Fig. 3b).
164 Comparison of the GTPBP5^{KO} and the GTPBP5^{IP} structures with the mature mt-LSU reveals
165 extensive maturation of the PTC upon GTPBP5 binding. The partly unfolded H89 in the
166 GTPBP5^{KO} is folded in the GTPBP5^{IP} (Fig. 3 b1). This folding is coordinated by the joint action
167 of GTPBP5 and NSUN4: in the presence of GTPBP5, the extended N-terminal region of
168 NSUN4 inserts into the rRNA core and temporarily displaces the P-loop (Fig. 3 b2), thereby

169 breaking the P-loop interaction with H89 (Fig. 3d). As a consequence, H89 is given the space
170 necessary to fold into a structure similar to its mature form (Fig. 3 b1, lower).
171 The GTPBP5^{IP} structure shows a rotation of the L7/L12 stalk in comparison to the GTPBP5^{KO}
172 structure (Extended Data Fig. 6c). Here, the rRNA in the L54/L11 region of the stalk forms π-
173 stacking interactions with two residues of the GTP-ase switch I element of GTPBP5 (Extended
174 Data Fig. 6a,c). Thereby, the L7/L12 stalk stabilizes the "state 2" conformation of the switch I.
175 In this way, the rotated L7/L12 stalk stabilizes the GTP-state of GTPBP5[26] and consequently a
176 GTP is bound in our structure (Extended Data Fig. 6a,c). The requirement for GTPBP5 to be in
177 a GTP-bound state is supported by the inability of a GTPBP5 Walker A mutant (GTPBP5-
178 S238A) to bind mt-LSU intermediates [8]. A back-rotation of the L7/12 stalk, presumably by
179 binding of another maturation factor to the mt-LSU assembly intermediate, would lead to a
180 release of the switch I and the activation of GTP hydrolysis, followed by release of GTPBP5
181 from the mt-LSU assembly intermediate. Taken together, GTPBP5 plays a direct and active
182 role in rRNA remodeling and, together with the NSUN4 N-terminus, orchestrates the
183 maturation of mitoribosomal PTC.
184

185 **Translation elongation factor mtEF-Tu is involved in mitoribosome assembly**

186 mtEF-Tu consists of a GTPase domain (G-domain; domain I) and two structurally
187 similar β-stranded domains (domains II and III) (Fig. 4a). It was recently shown that during
188 translation, mtEF-Tu·GTP delivers aminoacylated-tRNA to the mitoribosome in a manner
189 similar to its bacterial EF-Tu counterparts (Extended Data Fig. 7a,[27]). In contrast, the binding
190 of an EF-Tu·GTP·aa-tRNA complex is sterically hindered by the MALSU1 module bound in
191 our mt-LSU intermediates (Extended Data Fig. 7a). Unexpectedly, mtEF-Tu binds to the
192 mitoribosome in a unique manner in our GTPBP5^{IP} structure (Fig. 4b). Here, domains II and
193 III establish extensive interactions with GTPBP5, the sarcin-ricin loop (SRL) and the MALSU1
194 stalk (Fig. 4b,c). In addition, the G-domain switch I element, in its "state 1"/GDP conformation
195 (Extended Data Fig. 7b), extends and binds MALSU1. Thereby, mtEF-Tu, together with the
196 SRL and MALSU1, forms a platform for GTPBP5 binding (Fig. 4b). These structural
197 conclusions are supported by earlier mass-spectrometry data on isolated GTPBP5^{IP} assembly
198 intermediates and protein-proximity interactome analysis [8,28].
199 The G-domain of mtEF-Tu does not contact the SRL as in mtEF-Tu's canonical role in
200 translation but instead binds to the C-terminal region of a bL12m that also contacts uL10m at
201 the stalk base (Fig. 4b). In bacteria, homologs to bL12m and uL10m, recruit and activate

202 translational GTPases such as EF-Tu via the bL12m C-terminal domain[29,30] and stimulate GTP
203 hydrolysis 1000-fold[31]. Taken together, this suggests that mtEF-Tu hydrolysis – stimulated by
204 bL12m and uL10m – is used to accommodate GTPBP5 on the maturating mt-LSU in analogy
205 to the canonical EF-Tu role in translation, in which aminoacylated-tRNA is accommodated on
206 the translating ribosome (Extended Data Fig. 7a).
207
208 **Concluding remarks**
209 Our analyses shed new light into mammalian mitoribosome maturation and explain the
210 essential roles of several assembly factors that together promote fine RNA rearrangments and
211 lead to the mt-LSU completion. Thanks to our approaches that combine biochemical tools with
212 structural determination, we were able to uncovered several features unique to mammalian
213 mitochondria. Based on these data, we propose a model of the late-stage mt-LSU assembly that
214 requires the interplay of nine auxiliary factors (Fig. 4d).
215 Lastly, as defects in mitoribosome biogenesis – resulting from, for example, mutations
216 in MRM2 and GTPBP5 – are increasingly implicated in mitochondrial disease [32,33], the current
217 work does not only describes fundamental cellular processes but may also further new
218 diagnostic and therapeutic approaches to mitochondrial diseases.
219
220 **Methods**
221
222 **Generation of GTPBP5 knock-out cell line**
223 The knock-out cell line (GTPBP5^{KO}) was generated in the Flp-In T-Rex human embryonic
224 kidney 293 (HEK293T) cell line (Invitrogen) using CRISPR/Cas9 technology targeted on exon
225 1 of *MTG2* gene, which encodes for GTPBP5, as described [8]. In short, two pairs of gRNAs
226 were designed and cloned into the pSpCas9(BB)-2A-Puro (pX459) V2.0 vector to generate out-
227 of-frame deletions. Transfection of HEK293T cell line with the pX459 variants was performed
228 using Lipofectamine 3000 following manufacturer's instructions. Selection of transfected cells
229 was done using puromycin treatment at a final concentration of 1.5 mg/ml for 48 hours.
230 Subsequently, cells were single-cell diluted and transferred into a 96-well plate. Selected
231 clones were screened via Sanger sequencing and Western blotting.
232
233 **Purification of the mt-LSU from GTPBP5^{KO} cell line via sucrose gradient centrifugation**
234 Isolation of mitochondria was performed from GTPBP5^{KO} cell line as described in Rorbach *et*
235 *al.* [24], with some modifications. Crude mitochondria were further purified via differential

236 centrifugation by being loaded onto a sucrose gradient (1 M and 1.5 M sucrose, 20 mM Tris-
237 HCl pH 7.5, 1 mM EDTA) and centrifuged at 25000 rpm for 1 hour at 4°C (Beckman Coulter
238 SW41-Ti rotor). Mitochondria forming a band at the interphase between the 1 M and 1.5 M
239 sucrose were collected and resuspended in 10 mM Tris-HCl pH = 7.5 in 1:1 ratio. After
240 centrifugation, the final mitochondrial pellet was resuspended in mitochondrial freezing
241 buffer (200 mM trehalose, 10 mM Tris-HCl pH 7.5, 10 mM KCl, 0.1% BSA, 1 mM EDTA),
242 snap frozen in liquid nitrogen and stored at -80°C.
243 The mt-LSU was purified from the GTPBP5^{KO} cell line via a sucrose gradient centrifugation
244 experiment. Mitochondria were lysed at 4°C for 20 minutes (25 mM HEPES-KOH pH = 7.5,
245 20 mM $Mg(OAc)_2$, 100 mM KCl, 2% (v/v) Triton X-100, 2 mM dithiothreitol (DTT), 1x
246 cOmplete EDTA-free protease inhibitor cocktail (Roche), 40 U/µl RNase inhibitor
247 (Invitrogen)) and later centrifuged at 13000 rpm for 5 minutes at 4°C. For mitoribosome
248 purification, the mitolysate was subjected to sucrose cushion ultracentrifugation method (0.6
249 M sucrose, 25 mM HEPES-KOH pH = 7.5, 10 mM $Mg(OAc)_2$, 50 mM KCl, 0.5% (v/v) Triton
250 X-100, 2 mM DTT) by being centrifuged at 73000 rpm for 45 minutes at 4°C (Beckman Coulter
251 TL120.2 rotor). The mitoribosomal pellet was subsequently resuspended in ribosome
252 resuspension buffer (25 mM HEPES-KOH pH = 7.5, 10 mM $Mg(OAc)_2$, 50 mM KCl, 0.05%
253 DDM, 2 mM DTT) and centrifuged at 13000 rpm for 10 minutes at 4°C. The obtained
254 supernatant was then loaded onto a linear sucrose gradient (15-30% (w/v)) in 1x gradient buffer
255 (25 mM HEPES-KOH pH = 7.5, 10 mM $Mg(OAc)_2$, 50 mM KCl, 0.05% DDM, 2 mM DTT)
256 and centrifuged for 2 hours and 15 minutes at 39000 rpm at 4°C (Beckman Coulter TLS55
257 rotor). Fractions corresponding to the large mitochondrial subunit were collected and subjected
258 to buffer exchange (25 mM HEPES-KOH pH = 7.5, 10 mM $Mg(OAc)_2$, 50 mM KCl) using
259 Vivaspin 500 centrifugal concentrators.
260
261 **Generation of a mammalian cell line expressing GTPBP5**
262 A stable mammalian cell line overexpressing C-terminal FLAG-tagged GTPBP5
263 (GTPBP5::FLAG) in a doxycycline-inducible dose-dependent manner was generated as
264 described in Cipullo et al. [8]. The GTPBP5 cDNA (hORFeome Database; Internal ID: 12579)
265 was cloned into pcDNA5/FRT/TO. Flp-In T-Rex human embryonic kidney 293 (HEK293T,
266 Invitrogen) cells were cultured in DMEM (Dulbecco's modified eagle medium) containing 10%
267 (v/v) tetracycline-free fetal bovine serum (FBS), 2 mM Glutamax (Gibco), 1x
268 Penicillin/Streptomycin (Gibco), 50 µmg/ml uridine, 10 µg/ml Zeocin (Invitrogen) and 100
269 µg/ml blasticidin (Gibco) at 37 °C under 5% CO_2 atmosphere. Cells were seeded in a 6-well

270 plate, grown in medium without antibiotics and co-transfected with pcDNA5/FRT/TO-
271 GTPBP5::FLAG and pOG44 using Lipofectamine 3000 according to manufacturer's
272 recommendations. After 48 hours, selection of cells was promoted by addition of hygromycin
273 (100 µg/ml, Invitrogen) and blasticidin (100 µg/ml) to culture media. After two to three weeks
274 post-transfection, single colonies were picked and GTPBP5 overexpression was tested via
275 Western Blot analysis 48 hours after induction with 50 ng/ml doxycycline.
276
277 **Immunoprecipitation experiment**
278 Isolation and purification of mitochondria from GTPBP5::FLAG overexpressing cell line was
279 performed as described in the above paragraph "Purification of the mt-LSU from GTPBP5^{KO}
280 cell line via sucrose gradient centrifugation". The mt-LSU bound with GTPBP5 was isolated
281 via FLAG-immunoprecipitation analysis (IP). Pelleted mitochondria were lysed at 4°C for 20
282 minutes (25 mM HEPES-KOH pH = 7.5, 20 mM $Mg(OAc)_2$, 100 mM KCl, 2% (v/v) Triton X-
283 100, 0.2 mM DTT, 1x cOmplete EDTA-free protease inhibitor cocktail (Roche), 40 U/□l
284 RNase inhibitor (Invitrogen)) and centrifuged at 5000g for 5 minutes at 4°C. The supernatant
285 was then added to ANTI-FLAG M2-Agarose Affinity Gel (Sigma-Aldrich) previously
286 equilibrated (25 mM HEPES-KOH pH = 7.5, 5 mM $Mg(OAc)_2$, 100 mM KCl, 0.05% DDM)
287 and incubated for 3 hours at 4°C. After incubation, the sample was centrifuged at 5000g for 1
288 minute at 4°C, the supernatant was removed and the gel was washed three times with wash
289 buffer. Elution (25 mM HEPES-KOH pH = 7.5, 5 mM $Mg(OAc)_2$, 100 mM KCl, 0.05% DDM,
290 2 mM DTT) was performed using 3x FLAG Peptide (Sigma-Aldrich) for about 40 minutes at
291 4°C.
292
293 **Cryo-EM data acquisition and image processing**
294 Prior to cryo-EM grid preparation, grids were glow-discharged with 20 mA for 30 seconds
295 using a PELCO easiGlow glow-discharge unit. Quantifoil Cu 300 mesh (R 2/2 geometry;
296 Quantifoil Micro Tools GMBH) covered with a thin layer of 3 nm carbon were used for the for
297 the GTPBP5^{KO} sample. Carbon lacey films (400 mesh Cu grid; Agar Scientific) mounted with
298 ultrathin carbon support film were used for the GTPBP5^{IP} sample. Three □l aliquots of sample
299 were applied to the grids, which were then vitrified in a Vitrobot Mk IV (Thermo Fisher
300 Scientific) at 4°C and 100% humidity (blot 10 s, blot force 3, 595 filter paper (Ted Pella Inc.)).
301 Cryo-EM data collection (Extended Data Table 1) was performed with EPU (Thermo Fisher
302 Scientific) using a Krios G3i transmission-electron microscope (Thermo Fisher Scientific)
303 operated at 300 kV in the Karolinska Institutet's 3D-EM facility. Images were acquired in

304 nanoprobe EFTEM SA mode with a slit width of 10 eV using a K3 Bioquantum during 1 second
305 during which 60 movie frames were collected with a flux of 0.82 $e^{-}/Å^{2}$ per frame. Motion
306 correction, CTF-estimation, Fourier binning (to 1.02 Å/px), picking and extraction in 600 pixel
307 boxes (size threshold 300 Å, distance threshold 20 Å, using the pretrained
308 BoxNet2Mask_20180918 model) were performed on the fly using Warp [34]. Only particles from
309 micrographs with an estimated resolution of 3.6 Å and underfocus between 0.2 and 3 □m were
310 retained for further processing.
311 For the $GTPBP5^{KO}$ dataset, 704720 particles were picked from 37307 micrographs (Extended
312 Data Fig. 1). The particles were imported into CryoSPARC 2.15 [35] for further processing. After
313 2D classification, 130289 particles were selected for an ab-initio reconstruction. This
314 reconstruction, in addition to two "bad" reconstructions created from bad 2D class-averages,
315 were used for heterogeneous refinement of the complete particle set resulting in one of the three
316 classes yielding a large-subunit reconstruction with high resolution features (196318 particles).
317 After homogeneous refinement of these particles, the PDB model of a mitochondrial LSU
318 assembly intermediate (PDB: 5OOL [20]) was fitted in the density. The reconstruction contained
319 the MALSU1 module and also featured weak unexplained densities for several additional
320 components in the intersubunit interface. A 3D variability analysis was performed with a mask
321 on the intersubunit interface and a low pass resolution of 10 Å, and subsequently used for
322 clustering into six particle classes representing different assembly intermediates. Two of the
323 classes (43057 and 41619 particles) lacked the density for the A- and P-loops, H89, helices 68-
324 71 and the L7/12 stalk. The A- and P-loops become visible in the third class (28001 particles).
325 The fourth class revealed a number of biogenesis factors: MRM2, MTERF4-NSUN4, MTG1
326 and the structured H67-H71 rRNA region (helix-X) (48646 particles) as well as H89. All the
327 biogenesis factors are absent in the fifth class, in which helices 68 and 71 move to the mature
328 position (26678 particles). H69 is nevertheless not visible. The last class contains the small
329 subunit (8317 particles). Non-uniform refinement of the fourth particle set yielded a
330 reconstruction at 2.64. Å, which was used for model building and refinement. As the density
331 for MTG1 was weaker than for the other factors, 3D variability analysis was performed with a
332 mask on the MTG1 region and a 10 Å low-pass filter to select particles containing MTG1
333 (19254 particles, which was subsequently subjected to homogeneous refinement yielding a
334 reconstruction at 2.90 Å).
335 For the $GTPBP5^{IP}$ dataset, 283598 particles were picked from 112076 micrographs using
336 WARP and imported into CryoSPARC 2.15 (Extended Data Fig. 2) [35]. The complete particle
337 set was used in heterogeneous refinement against the same three references derived from the

338 GTPBP5^{KO} dataset. One of the classes (78306 particles) yielded a high-resolution
339 reconstruction of the mt-LSU assembly intermediate. After homogeneous refinement,
340 additional density for GTPBP5 was visible in the intersubunit interface. 3D variability analysis
341 was performed with a mask on the GTPBP5 region and a low pass resolution of 10 Å.
342 Subsequent clustering into two particle clusters revealed a particle subset containing GTPBP5
343 (71834 particles), which was used for model building and refinement. This reconstruction also
344 features densities for MRM2 and MTERF4-NSUN4. In addition, a weak density was present
345 for mtEF-TU, the bL12m C-terminal domain and MTG1. The refined particles were subject to
346 2D classification and the bad classes were removed. The remaining particles were polished and
347 refined in Relion 3.1 and re-imported into CryoSPARC for further processing. 3D variability
348 analysis was performed on these particles with a mask covering mtEF-TU, bL12m and MTG1
349 and a 10 Å low pass filter. Subsequent clustering (4 clusters) revealed 2 clusters containing
350 mtEF-TU/bL12m (17886 particles in total), one cluster containing MTG1 (8233 particles) and
351 one cluster containing all three proteins (13376 particles). The reconstructions derived from the
352 MTG1- and the mtEF-Tu-containing particles reached a resolution of 3.19 and 3.21 Å
353 respectively.
354
355 **Model building and refinement**
356 Model building of the GTPBP5^{KO} and GTPBP5^{IP} mt-LSU assembly intermediate structures was
357 performed using *Coot* [36]. The structure of a previous mt-LSU assembly intermediate (PDB
358 5OOL, [20]) was used as a starting model. MRM2 and MTERF4-NSUN4 were identified by
359 modelling secondary structure elements in *Coot*, and using the initial models for a structural
360 search using the DALI server [37]. MTG1, as well as mtEF-Tu and the bL12m C-terminal domain
361 in the GTPBP5-bound mt-LSU dataset, were identified using a density-based fold-recognition
362 pipeline [20]. Using SWISS-MODEL [38], we generated homology models for the human GTPBP5
363 (template: PDB 4CSU chain 9 [25]), MTG1 (template: PDB 3CNL chain A [39]), bL12m (template:
364 PDB 1DD3 chain A [40]) and mtEF-TU (template: PDB 1D2E chain A [41]). All the models, as
365 well as the crystal structure of the human MTERF4-NSUN4 (template: PDB 4FP9 chains A
366 and B [18]), were fitted into the density map using *Coot* JiggleFit. The MTG1 GTPase domain
367 and the L17/12 stalk were excluded from atomic refinement and were only subject to rigid body
368 refinement. Metal ions and modifications were placed based on map densities. Stereochemical
369 refinement was performed using PHENIX [42]. Refinement statistics are reported in Extended
370 Data Table 2, while modeled proteins and rRNA are shown in Extended Data Table 3.

371 Validation of the final models was done via MolProbity [43]. Figures were generated using
372 ChimeraX [44].
373
374 **References**

375 1. Hällberg, B. M. & Larsson, N.-G. Making Proteins in the Powerhouse. *Cell Metab.* **20**,
376 226–240 (2014).
377 2. Greber, B. J. *et al.* The complete structure of the 55S mammalian mitochondrial
378 ribosome. *Science (80-.).* **348**, 303–308 (2015).
379 3. Jaskolowski, M. *et al.* Structural Insights into the Mechanism of Mitoribosomal Large
380 Subunit Biogenesis. *Mol. Cell* **79**, 629-644.e4 (2020).
381 4. Saurer, M. *et al.* Mitoribosomal small subunit biogenesis in trypanosomes involves an
382 extensive assembly machinery. *Science (80-.).* **365**, 1144–1149 (2019).
383 5. Perez Boerema, A. *et al.* Structure of the chloroplast ribosome with chl-RRF and
384 hibernation-promoting factor. *Nat. Plants* **4**, 212–217 (2018).
385 6. Amunts, A., Brown, A., Toots, J., Scheres, S. H. W. & Ramakrishnan, V. The structure
386 of the human mitochondrial ribosome. *Science (80-.).* **348**, 95–98 (2015).
387 7. Bogenhagen, D. F., Ostermeyer-Fay, A. G., Haley, J. D. & Garcia-Diaz, M. Kinetics
388 and Mechanism of Mammalian Mitochondrial Ribosome Assembly. *Cell Rep.* **22**,
389 1935–1944 (2018).
390 8. Cipullo, M. *et al.* Human GTPBP5 is involved in the late stage of mitoribosome large
391 subunit assembly. *Nucleic Acids Res.* (2020) doi:10.1093/nar/gkaa1131.
392 9. Lavdovskaia, E. *et al.* The human Obg protein GTPBP10 is involved in mitoribosomal
393 biogenesis. *Nucleic Acids Res.* **46**, 8471–8482 (2018).
394 10. Maiti, P., Kim, H.-J., Tu, Y.-T. & Barrientos, A. Human GTPBP10 is required for
395 mitoribosome maturation. *Nucleic Acids Res.* (2018) doi:10.1093/nar/gky938.
396 11. Maiti, P., Antonicka, H., Gingras, A.-C., Shoubridge, E. A. & Barrientos, A. Human
397 GTPBP5 (MTG2) fuels mitoribosome large subunit maturation by facilitating 16S
398 rRNA methylation. *Nucleic Acids Res.* **48**, 7924–7943 (2020).
399 12. Kim, H.-J. & Barrientos, A. MTG1 couples mitoribosome large subunit assembly with
400 intersubunit bridge formation. *Nucleic Acids Res.* **46**, 8435–8453 (2018).
401 13. Lavdovskaia, E. *et al.* Dual function of GTPBP6 in biogenesis and recycling of human
402 mitochondrial ribosomes. *Nucleic Acids Res.* **48**, 12929–12942 (2020).
403 14. Brown, A. *et al.* Structure of the large ribosomal subunit from human mitochondria.
404 *Science (80-.).* **346**, 718–722 (2014).

405 15. Aibara, S., Singh, V., Modelska, A. & Amunts, A. Structural basis of mitochondrial
406 translation. *Elife* **9**, (2020).
407 16. Cámara, Y. *et al.* MTERF4 Regulates Translation by Targeting the Methyltransferase
408 NSUN4 to the Mammalian Mitochondrial Ribosome. *Cell Metab.* **13**, 527–539 (2011).
409 17. Metodiev, M. D. *et al.* NSUN4 Is a Dual Function Mitochondrial Protein Required for
410 Both Methylation of 12S rRNA and Coordination of Mitoribosomal Assembly. *PLoS*
411 *Genet.* **10**, e1004110 (2014).
412 18. Spåhr, H., Habermann, B., Gustafsson, C. M., Larsson, N.-G. & Hallberg, B. M.
413 Structure of the human MTERF4–NSUN4 protein complex that regulates
414 mitochondrial ribosome biogenesis. *Proc. Natl. Acad. Sci.* **109**, 15253–15258 (2012).
415 19. Yakubovskaya, E. *et al.* Structure of the Essential MTERF4:NSUN4 Protein Complex
416 Reveals How an MTERF Protein Collaborates to Facilitate rRNA Modification.
417 *Structure* **20**, 1940–1947 (2012).
418 20. Brown, A. *et al.* Structures of the human mitochondrial ribosome in native states of
419 assembly. *Nat. Struct. Mol. Biol.* **24**, 866–869 (2017).
420 21. Kim, H. J. & Barrientos, A. MTG1 couples mitoribosome large subunit assembly with
421 intersubunit bridge formation. *Nucleic Acids Res.* **46**, 8435–8453 (2018).
422 22. Seffouh, A. *et al.* Structural consequences of the interaction of RbgA with a 50S
423 ribosomal subunit assembly intermediate. *Nucleic Acids Res.* **47**, 10414–10425 (2019).
424 23. Lee, K. W. & Bogenhagen, D. F. Assignment of 2′-O-methyltransferases to
425 modification sites on the mammalian mitochondrial large subunit 16 S ribosomal RNA
426 (rRNA). *J. Biol. Chem.* **289**, 24936–24942 (2014).
427 24. Rorbach, J. *et al.* MRM2 and MRM3 are involved in biogenesis of the large subunit of
428 the mitochondrial ribosome. *Mol. Biol. Cell* **25**, 2542–2555 (2014).
429 25. Feng, B. *et al.* Structural and Functional Insights into the Mode of Action of a
430 Universally Conserved Obg GTPase. *PLoS Biol.* **12**, e1001866 (2014).
431 26. Matsumoto, S. *et al.* Molecular Mechanism for Conformational Dynamics of Ras·GTP
432 Elucidated from In-Situ Structural Transition in Crystal. *Sci. Rep.* **6**, 25931 (2016).
433 27. Desai, N. *et al.* Elongational stalling activates mitoribosome-associated quality control.
434 *Science (80-.).* **370**, 1105–1110 (2020).
435 28. Antonicka, H. *et al.* A High-Density Human Mitochondrial Proximity Interaction
436 Network. *Cell Metab.* **32**, 479-497.e9 (2020).
437 29. Traut, R. R. *et al.* Location and domain structure of Escherichia coli ribosomal protein
438 L7/L12: site specific cysteine cross-linking and attachment of fluorescent probes.

439 *Biochem. Cell Biol.* **73**, 949–958 (1995).
440 30. Mustafi, M. & Weisshaar, J. C. Simultaneous Binding of Multiple EF-Tu Copies to
441 Translating Ribosomes in Live Escherichia coli. *MBio* **9**, (2018).
442 31. Diaconu, M. *et al.* Structural Basis for the Function of the Ribosomal L7/12 Stalk in
443 Factor Binding and GTPase Activation. *Cell* **121**, 991–1004 (2005).
444 32. Garone, C. *et al.* Defective mitochondrial rRNA methyltransferase MRM2 causes
445 MELAS-like clinical syndrome. *Hum. Mol. Genet.* **26**, 4257–4266 (2017).
446 33. Solomon, B. D. *et al.* De novo deletion of chromosome 20q13.33 in a patient with
447 tracheo-esophageal fistula, cardiac defects and genitourinary anomalies implicates
448 GTPBP5 as a candidate gene. *Birth Defects Res. Part A Clin. Mol. Teratol.* **91**, 862–
449 865 (2011).
450 34. Tegunov, D. & Cramer, P. Real-time cryo-electron microscopy data preprocessing with
451 Warp. *Nat. Methods* **16**, 1146–1152 (2019).
452 35. Punjani, A., Rubinstein, J. L., Fleet, D. J. & Brubaker, M. A. cryoSPARC: algorithms
453 for rapid unsupervised cryo-EM structure determination. *Nat. Methods* **14**, 290–296
454 (2017).
455 36. Emsley, P., Lohkamp, B., Scott, W. G. & Cowtan, K. Features and development of
456 Coot. *Acta Crystallogr. Sect. D Biol. Crystallogr.* **66**, 486–501 (2010).
457 37. Holm, L. DALI and the persistence of protein shape. *Protein Sci.* **29**, 128–140 (2020).
458 38. Arnold, K., Bordoli, L., Kopp, J. & Schwede, T. The SWISS-MODEL workspace: a
459 web-based environment for protein structure homology modelling. *Bioinformatics* **22**,
460 195–201 (2006).
461 39. Kim, D. J., Jang, J. Y., Yoon, H.-J. & Suh, S. W. Crystal structure of YlqF, a circularly
462 permuted GTPase: Implications for its GTPase activation in 50 S ribosomal subunit
463 assembly. *Proteins Struct. Funct. Bioinforma.* **72**, 1363–1370 (2008).
464 40. Wahl, M. C., Bourenkov, G. P., Bartunik, H. D. & Huber, R. Flexibility,
465 conformational diversity and two dimerization modes in complexes of ribosomal
466 protein L12. *EMBO J.* **19**, 174–186 (2000).
467 41. Andersen, G. R., Thirup, S., Spremulli, L. L. & Nyborg, J. High resolution crystal
468 structure of bovine mitochondrial EF-tu in complex with GDP. *J. Mol. Biol.* **297**, 421–
469 436 (2000).
470 42. Liebschner, D. *et al.* Macromolecular structure determination using X-rays, neutrons
471 and electrons: recent developments in Phenix. *Acta Crystallogr. Sect. D Struct. Biol.*
472 **75**, 861–877 (2019).

43. Chen, V. B. *et al.* MolProbity : all-atom structure validation for macromolecular crystallography. *Acta Crystallogr. Sect. D Biol. Crystallogr.* **66**, 12–21 (2010).
44. Goddard, T. D. *et al.* UCSF ChimeraX: Meeting modern challenges in visualization and analysis. *Protein Sci.* **27**, 14–25 (2018).
45. Rosenthal, P. B. & Henderson, R. Optimal Determination of Particle Orientation, Absolute Hand, and Contrast Loss in Single-particle Electron Cryomicroscopy. *J. Mol. Biol.* **333**, 721–745 (2003).
46. Baker, N. A., Sept, D., Joseph, S., Holst, M. J. & McCammon, J. A. Electrostatics of nanosystems: Application to microtubules and the ribosome. *Proc. Natl. Acad. Sci.* **98**, 10037–10041 (2001).
47. Greber, B. J. *et al.* The complete structure of the 55S mammalian mitochondrial ribosome. *Science (80-.).* **348**, 303–308 (2015).

Acknowledgments: All cryo-EM data used in this work were collected at the Karolinska Institutet's 3D-EM facility. The SciLifeLab cryo-EM facility (used for grid preparation and initial screening) is funded by the Knut and Alice Wallenberg, Family Erling Persson, and Kempe foundations. We acknowledge the support of: Knut and Alice Wallenberg Foundation (KAW 2018.0080) to B.M.H and J.R.; the Swedish Research Council (2018-3808) to B.M.H.; Karolinska Institutet and the Max Planck Institute to J.R. J.R. is a Fellow of the Knut and Alice Wallenberg Foundation (WAF 2017).

Author contributions: M.C. with A.K and J.R. help performed cell biology, biochemistry and sample preparations; G.V.G. and B.M.H. performed cryo-EM data collection; G.V.G. and B.M.H. processed data and determined structures; G.V.G. built and refined models with help from A.K. and B.M.H.; M.C. and G.V.G. wrote the manuscript with input from all authors; J.R. and B.M.H. oversaw the project and edited the manuscript.

Competing interests: Authors declare no competing interests.

506

507

508

509

510

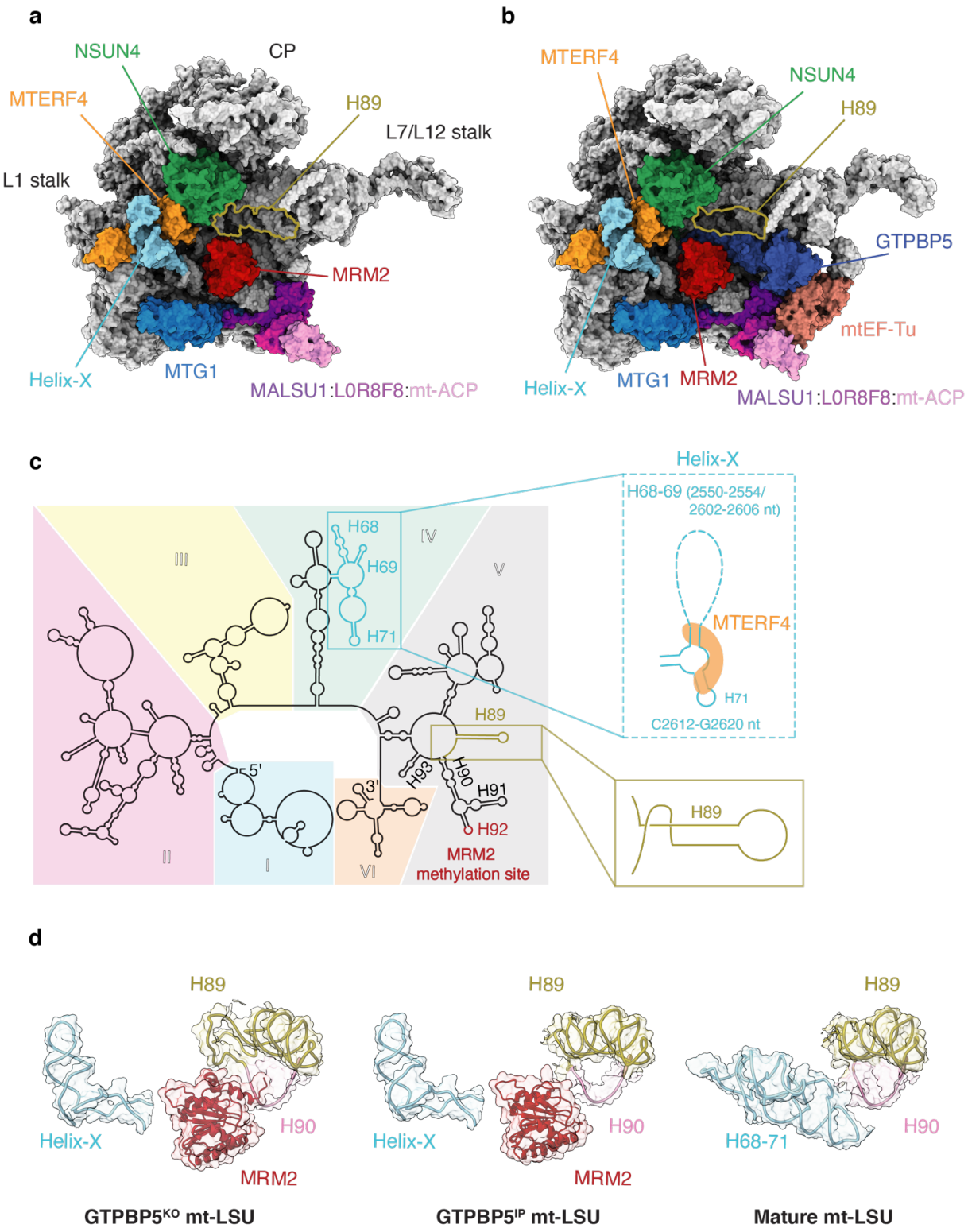

Fig. 1: Overview of the GTPBP5^{KO} and the GTPBP5^{IP} mt-LSU assembly intermediates and comparison with the mature mt-LSU. a, The GTPBP5^{KO} is bound by MTERF4, NSUN4, MRM2, MTG1 and the MALSU1 module. Mitoribosomal proteins and 16S mt-rRNA are shown in grey. Helix-X bound to MTERF4 is highlighted as well as H89. **b**, The interface of the GTPBP5^{IP} mt-LSU intermediate associated with MTERF4, NSUN4, MRM2, MTG1, MALSU1:L0R8F8:mt-ACP complex, GTPBP5 and mtEF-Tu. Helix-X bound to MTERF4 is shown in light blue. **c,** Secondary structure of the mature mt-LSU 16S mt-rRNA. Differences in the rRNA fold of

the GTPBP5^{KO} mt-LSU intermediate are shown in the zoomed-in views. Dashed lines indicate regions that are not modelled. MRM2 methylation site (H92) is indicated in red. The six 16S mt-rRNA domains are shown in different colours. **d**, Positioning of helix-X (H68-71) and helices H89 and H90 in GTPBP5^{KO} mt-LSU (left), GTPBP5^{IP} mt-LSU (middle) and the mature mt-LSU (right) (PDB:6ZSG [15]). In the GTPBP5^{KO} and the GTPBP5^{IP} mt-LSU structures MRM2 is present.

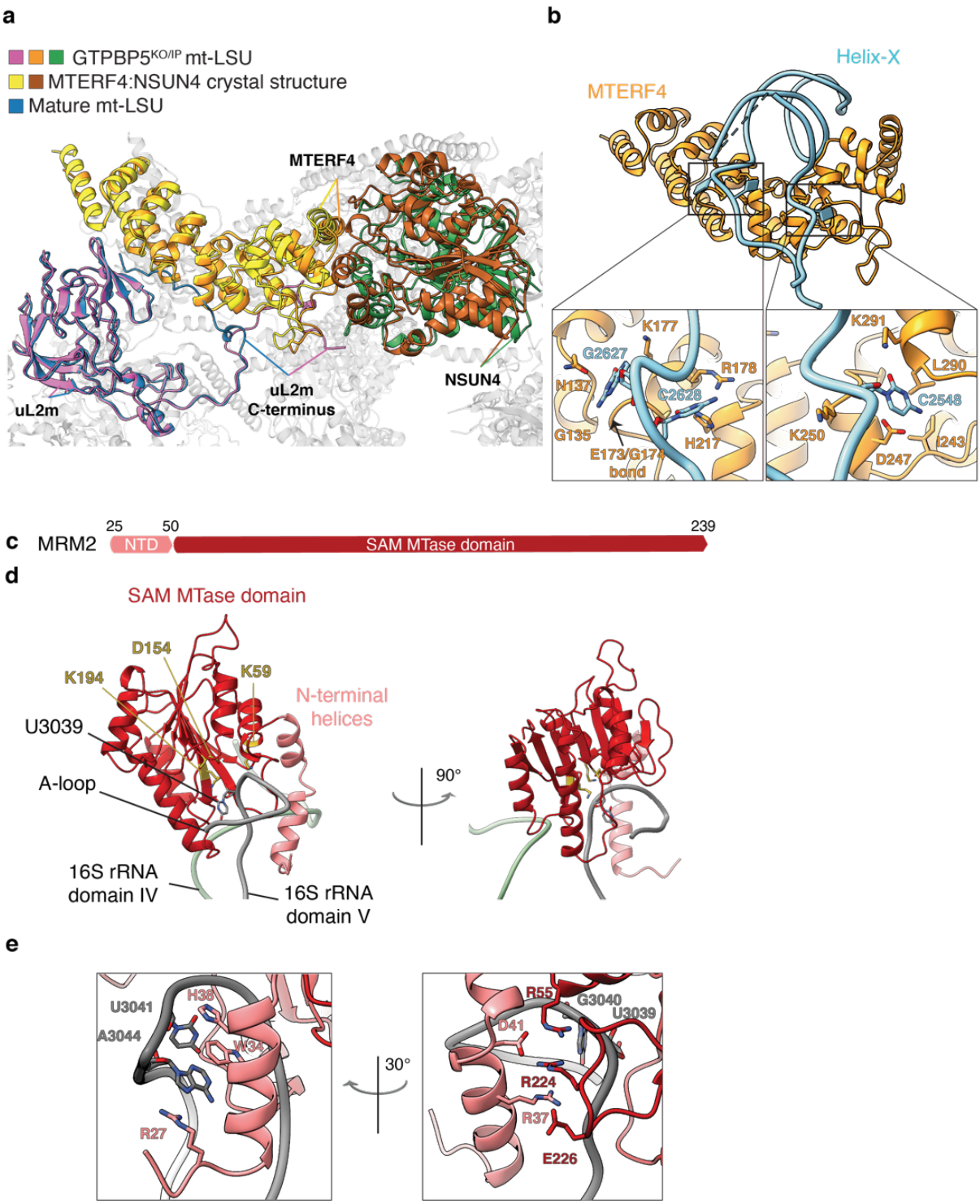

Fig. 2: MTERF4-NSUN4 and MRM2 interaction with the mt-LSU assembly intermediates. a, Comparison of the MTERF4-NSUN4 complex bound to the GTPBP5$^{KO/IP}$ mt-LSU (orange and green respectively) with the MTERF4-NSUN4 crystal structure (PDB: 4FP9 [18]) (yellow and brown, respectively), and of uL2m from the GTPBP5$^{KO/IP}$ mt-LSU (pink) with uL2m from the mature mt-LSU (blue) (PDB: 3J7Y [14]). The uL2m C-terminus is indicated in both structures. Helix-X is not shown. **b**, MTERF4-NSUN4 complex bound to helix-X. Zoom-in panels show the interactions of MTERF4 with helix-X. **c,** Schematic representation of MRM2 domains (NTD - light pink, SAM MTase domain - red). **d**, MRM2 interaction with the domain IV rRNA (nucleotides 2644-2652, green) and the A-loop (grey). The MRM2 methylation site (U3039) as well as the catalytic triad of MRM2 (K59,

550 D154, K194) are highlighted as sticks. **e**, Zoomed-in views showing MRM2 interactions with the A-loop in
551 different orientations.

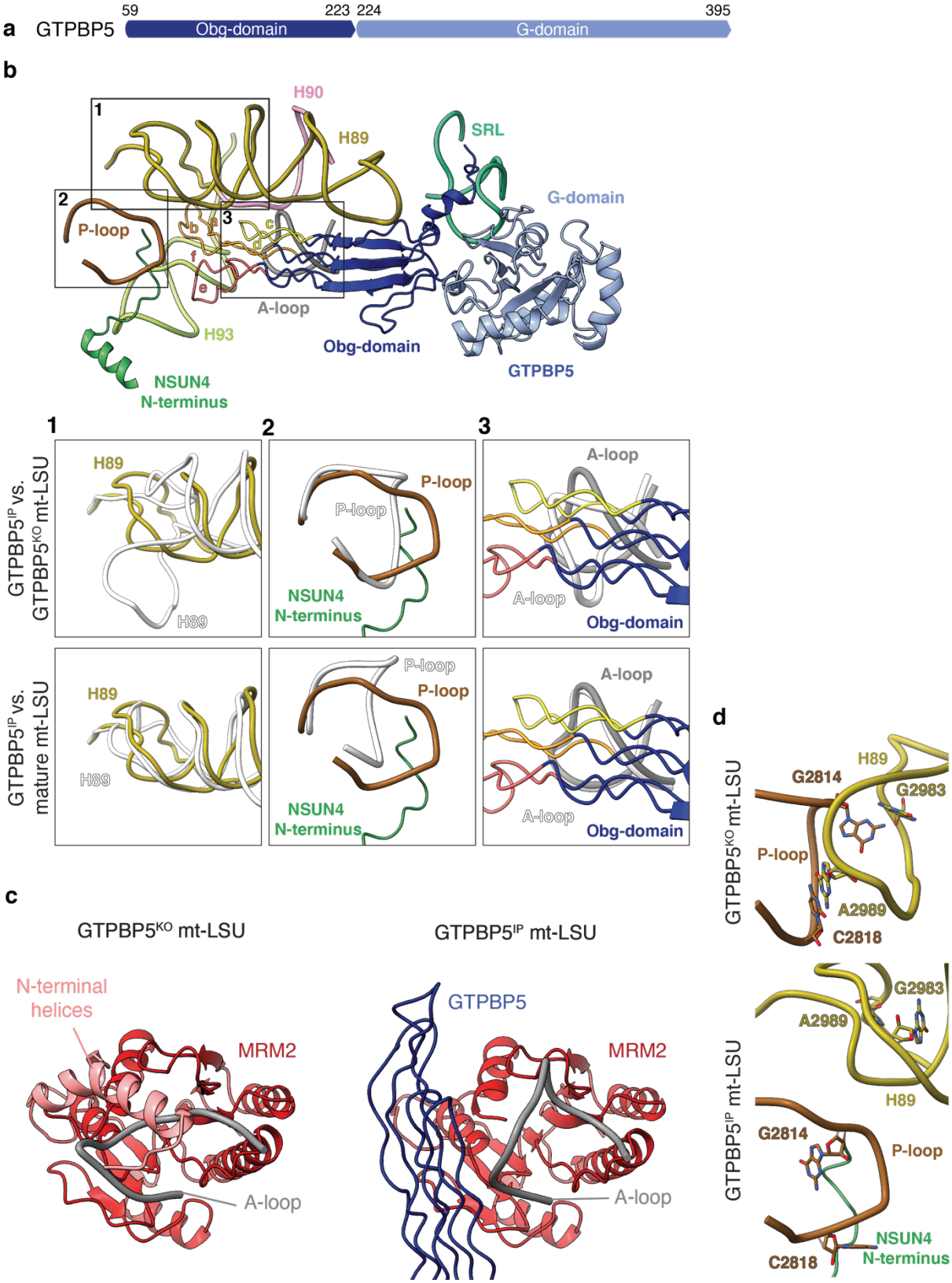

552

553 **Fig. 3: GTPBP5 contributes to the maturation of the PTC region. a**, Schematic representation of GTPBP5
554 domains (Obg-domain dark blue, G-domain light blue). **b**, Overview of GTPBP5 interactions with the 16S rRNA.
555 The Obg-domain (dark blue) contacts helices that are in the PTC region: P-loop, A-loop, H89, H90, H93. Helices

556 a-f of GTPBP5 Obg-domain are indicated. The SRL and the NSUN4 N-terminus are shown. Boxes 1-3 show the
557 remodelling of the PTC in GTPBP5^{IP} mt-LSU (in color) compared with GTPBP5^{KO} mt-LSU (in white, higher
558 panel) and with the mature mt-LSU (in white, lower panel) (PDB: 6ZSG[15]). **c**, Comparison of MRM2 (red) and
559 the A-loop (grey) conformations between GTPBP5^{KO} mt-LSU (left) and GTPBP5^{IP} mt-LSU (right). The N-
560 terminal helices (pink) of MRM2 could not be modelled in the GTPBP5^{IP} mt-LSU. The GTPBP5 Obg-domain is
561 shown in dark blue. **d**, Comparison of the P-loop and H89 conformations between GTPBP5^{IP} mt-LSU (lower
562 panel) and GTPBP5^{KO} mt-LSU structures (higher panel).

563

564

565

566

567

568

569

570

571

572

573

574

575

576

577

578

579

580

581

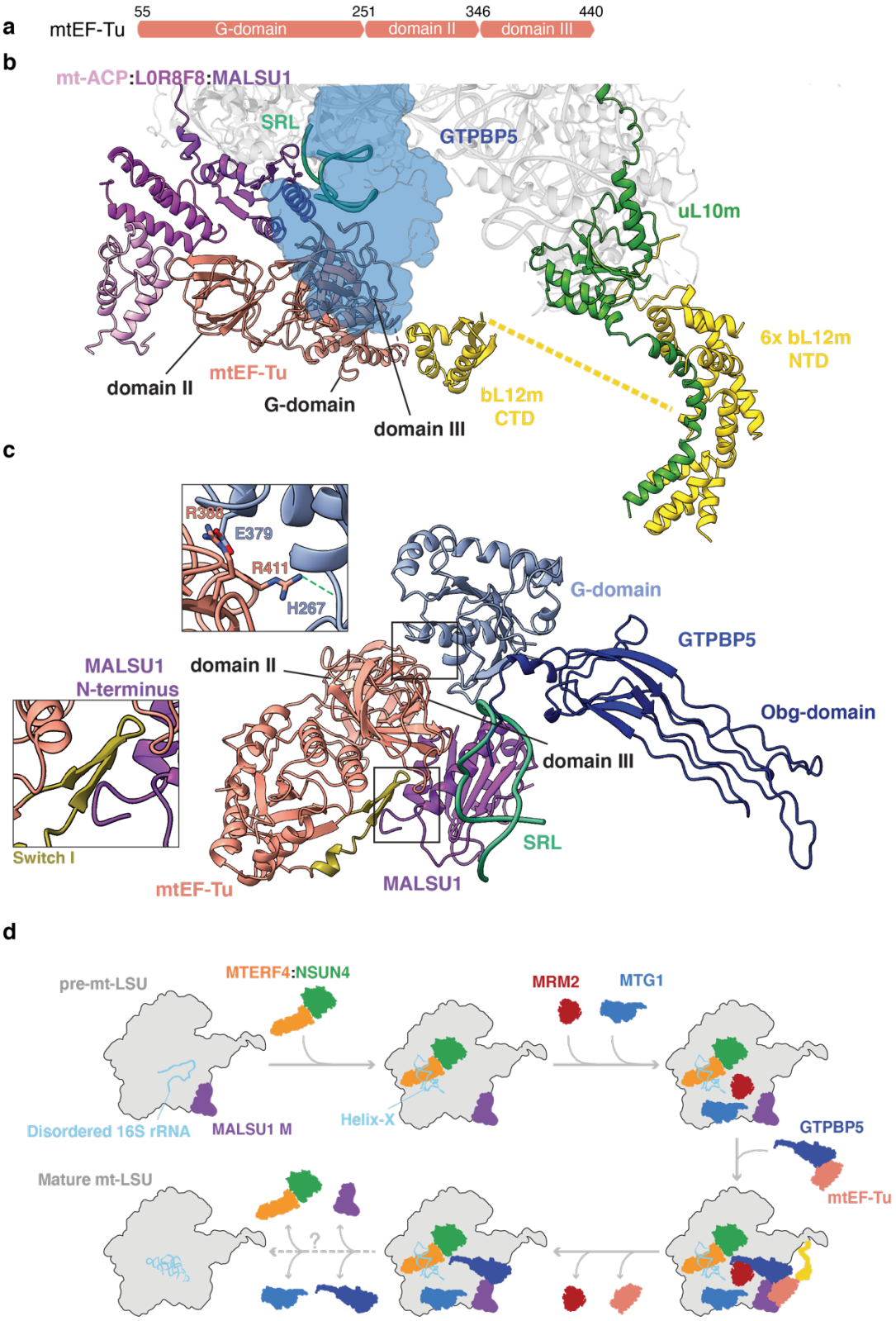

Fig. 4: Interaction of mtEF-Tu with the mt-LSU assembly intermediate and model of the final steps of mt-LSU biogenesis. a, Schematic representation of mtEF-Tu domains. **b**, mtEF-Tu interaction with GTPBP5, the MALSU1 module and the bL12m C-terminal domain. mtEF-Tu G-domain, domain II and domain III and the SRL are indicated. The six copies of bL12m N-terminal domain and uL10m are also highlighted. The yellow dashed

line indicates a hypothetical connection between bL12m CTD and one of the six copies of bL12m NTD, not visible in the structure. **c**, Representation of the mtEF-Tu interaction with GTPBP5 and MALSU1. The upper zoomed-in panel features interactions between the GTPBP5 G-domain and the mtEF-Tu domain III. The green dashed line indicates interactions to the RNA phosphate backbone. The lower zoomed-in panel shows the mtEF-Tu switch I interaction with MALSU1. **d**, Final steps of the mt-LSU assembly. The dashed arrow indicates that biogenesis factors are released in an unknown order.